Effects of confinement on the dynamics and correlation scales in kinesin-microtubule active fluids

Yi Fan [1], Kun-Ta Wu,[2] S. Ali Aghvami [3], Seth Fraden [3] and Kenneth S. Breuer[1,*]

[1]*Center for Fluid Mechanics, School of Engineering, Brown University, Providence, Rhode Island 02912, USA*
[2]*Department of Physics, Worcester Polytechnic Institute, Worcester, Massachusetts 01609, USA*
[3]*School of Physics, Brandeis University, Waltham, Massachusetts 02453, USA*

We study the influence of solid boundaries on dynamics and structure of kinesin-driven microtubule active fluids as the height of the container, H, increases from hundreds of micrometers to several millimeters. By three-dimensional tracking of passive tracers dispersed in the active fluid, we observe that the activity level, characterized by velocity fluctuations, increases as system size increases and retains a small-scale isotropy. Concomitantly, as the confinement level decreases, the velocity-velocity temporal correlation develops a strong positive correlation at longer times, suggesting the establishment of a "memory". We estimate the characteristic size of the flow structures from the spatial correlation function and find that, as the confinement becomes weaker, the correlation length, l_c, saturates at approximately 400 microns. This saturation suggests an intrinsic length scale which, along with the small-scale isotropy, demonstrates the multiscale nature of this kinesin-driven bundled microtubule active system.

I. INTRODUCTION

Active fluids, and more specifically, cytoskeletal networks of actin filaments or microtubules, exhibit large-scale nonequilibrium dynamics driven by mesoscopic active stresses, which are generated by nanoscale motion of molecular motors [1–6]. Boundaries can dramatically transform the dynamics of such cytoskeletal active networks generating coherent flow patterns or self-organized states including, for example vortical, spiral, swirling, and other patterns [7–13]. From a biological perspective, the formation of these patterns underlie biological phenomena such as spindle formation or cytoplasmic streaming [14–18], while from a more physical perspective, active fluids provide a novel system that converts chemical energy into mechanical work at the molecular scale and then generates mesoscopic activity at much larger scales, mediated by the short- and long-range interactions intrinsic to the specific active medium.

A particularly versatile model system of active fluids is composed of ~ 100 μm long bundles of short microtubule filament, each approximately 1.5 μm long. These bundles extend, buckle, and fray, driven by the motion of kinesin molecular motors [19]. Most of the studies of the isotropic active phase using this long-lasting active fluid have focused on two different configurations: two-dimensional unconfined thin-film and three-dimensional annular geometries. The thin-film systems are unconfined in the horizontal plane (*x-y*) and measure 100 μm or less in the vertical (*z*) axis. The vertical confinement is achieved either using an oil film or a solid boundary. This geometry has been used to characterize the dynamics and structure of the system for a variety of different microscopic constituents [20,21].

The second broad category of geometries are three-dimensional annular "race-tracks", which have a planform, or *x-y* geometry, in the form of a circle, square, ratchet, toroid, or long channel but are confined in the transverse, or *y-z* plane, by solid boundaries. Such confinement can transform the chaotic dynamics of three-dimensional (3D) bulk isotropic fluids into long-ranged and long-lived coherent flows and be capable of transporting materials over macroscopic scales [22,23]. The emergence of such coherent flows appears to be determined by a scale-invariant criterion that depends on the aspect ratio of the confining geometry.

To understand these effects, it is essential to elucidate the influence of the hard wall boundaries on the active fluid structure and dynamics and to quantify the changing length and time scales that emerge in response to confinement. In this work we report on the behavior of a 3D bulk active fluid system as it is subjected to decreasing confinement in one direction. To study this, we have conducted a series of experiments in cuboid channels whose horizontal dimension is large (2 or 4 mm) compared to any internal scale of the active medium, but whose vertical dimension, H, ranges from a highly confined geometry ($H = 100$ μm) to one whose scale is large and comparable to the horizontal system scale ($H > 2$ mm). In each of these test geometries (except the largest geometry case) we tracked passive tracer particles in all three dimensions and calculated their transport, spatial and temporal correlation in the active fluids.

II. MATERIALS AND METHODS

A. Active fluids

Active fluids composed of microtubule filaments, kinesin-streptavidin motor clusters, depletion agents (Pluronic F-127, Sigma, P2443), and an adenosine triphosphate (ATP) regeneration system. Pluronic micelles force the microtubule

*kenneth_breuer@brown.edu

TABLE I. Summary of experimental details for each channel. Channels i–vii have increasing chamber height, H, with the measurement position, $\Delta z/H$, at (approximately) the channel center. Channels vi-a and vi-b have the same dimensions as channel vi, but the observation position is closer to one of the boundaries.

Index number	Chamber dimension			Objective		Observation position		Tracer	
	W (mm)	L (mm)	H (mm)	WD (mm)	NA	Δz (mm)	$\Delta z/H$	diameter (μm)	Tracking dimensions
i	2.0	2.0	0.1	1.0	0.75	0.05	0.5	1.0	3D
ii	2.0	2.0	0.3	1.0	0.75	0.15	0.5	1.0	3D
iii	2.0	2.0	0.5	1.0	0.75	0.25	0.5	1.0	3D
iv	2.0	2.0	1.0	1.0	0.75	0.50	0.5	1.0	3D
v	2.0	2.0	1.5	1.0	0.75	0.75	0.5	1.0	3D
vi	2.0	2.0	2.0	1.0	0.75	0.80[a]	0.4	1.0	3D
vi-a	2.0	2.0	2.0	1.0	0.75	0.05	0.025	1.0	3D
vi-b	2.0	2.0	2.0	1.0	0.75	0.15	0.075	1.0	3D
vii	4.0	4.0	4.0	6.9	0.45[b]	2.00	0.5	2.9	2D

[a]Objective Nikon CFI Plan Apo VC 20×. Its working distance (WD) restricted the observation position Δz.
[b]Objective Nikon CFI S Plan Fluor ELWD 20×. Its numerical aperture (NA) restricted the tracking dimension to two-dimensional.

filaments to form bundles [24]. Kinesin-streptavidin motor clusters simultaneously bind to and walk along neighbor microtubule filaments, inducing a sliding motor force between antipolar filaments. The active stress generated by thousands of molecular motors drives the system out of equilibrium. The ATP regeneration system maintains the ATP concentration in the active fluid which ensures that the kinesin motors step at constant speed for the duration of the experiment. All of the experiments presented here used an active fluid with a constant concentration of microtubules (1.3 mg/ml), kinesin (1.5 μM), and ATP (1.4 mM). Complete details on the active material preparation are described in Appendix A. We dispersed ~0.001% (v/v) spherical colloidal fluorescent tracers (2.9 μm diameter, 395 nm/428 nm, Bangs Laboratories, or 1 μm diameter, 412 nm/447 nm, Thermal Fisher Scientific) in the active fluid, with the tracer size determined by the channel size and target observation region.

B. Test enclosure

Test chambers, consisting of a rectangular cavity measuring 2 by 2 mm (x-y), with a height (z) that varied from $H = 100$ μm to 2 mm [Table I (i–vi)] and a cube measuring 4 mm in each of the three dimensions [Table I (vii)] were fabricated from cyclic olefin copolymer (COC) sheets using a CNC mill (MDA Precision LLC, Model V8-TC8 3-axis). The active fluids were loaded into the chamber which was then sealed using a glass slide (Fisher scientific, 12-542C). To ensure a consistent surface condition, all channels and cover slides were coated with polyacrylamide before experiments [19,20] (see Appendix B). The assembly was held onto the microscope stage by a machined aluminum plate with a poly-dimethylsiloxane layer (~1-mm thickness placed between the glass and aluminum to provide stress relief).

C. Measurement procedures

An epifluorescence microscope (Nikon TE 200 eclipse) equipped with a z-scanning system (Piezo z-drive, Physik Instrumente, Model P-725) was used to observe the motion of the fluorescent tracers. Light from a high power LED source (405 nm, Thorlabs, DC4100) was directed through a narrow-band filter to an air immersion objective (either Nikon CFI S Plan Fluor ELWD 20×, NA = 0.45, WD = 6.9 mm or Nikon CFI Plan Apo VC 20×, NA = 0.75, WD = 1.0 mm). The emission from the fluorescent tracers was directed through a narrow-band emission filter and recorded using an sCMOS camera (PCO-Tech, PCO edge 5.5, 2560 × 2160 pixels) at 10 Hz.

Tracer particles in the focal plane appear as sharp spots in the camera image while particles located away from the focal plane appear as "Airy rings" [25] whose diameter can be accurately correlated with the particle position above or below the focal plane [26,27] [Figs. 1(a) and 1(b)]. A typical image contained 30 particles, each of which was tracked in three dimensions using its position in the image and the size of the tracer's point spread function. The ring size was determined using a Sobel edge detection algorithm and the Circle Hough Transform [28,29] [Figs. 1(c) and 1(d)]. A reference library, which relates the Airy ring size to the tracer's distance from the focal plane, was built [Fig. 1(e)] by z-scanning a 1-μm tracer particle immobilized in agarose gel with 0.1-μm intervals using the piezo z-drive. The agarose gel is 1% (w/w) with the same refractive index as the active fluid medium. Although it has a weblike structure, the underlying microtubule network is dilute and spatially homogeneous and can be safely considered to be optically uniform. The Airy rings recorded are uniform in intensity and are circular (See Supplemental Material videos 1 and 2 [30]), confirming that there is no optical distortion that would be introduced by spatial variations in the optical properties of the active fluid. The resultant measurement and tracking system could determine the tracer location within a 350 μm × 350 μm × ~40μm observation volume, with an accuracy of 0.2 μm in the x-y plane and 0.4 μm in the z direction. For the largest geometry [channel vii, Table I], the large value of H required the use of a microscope objective with a long working distance. For this case, the numerical aperture did not allow for detection of the Airy rings and restricted the particle tracking to two
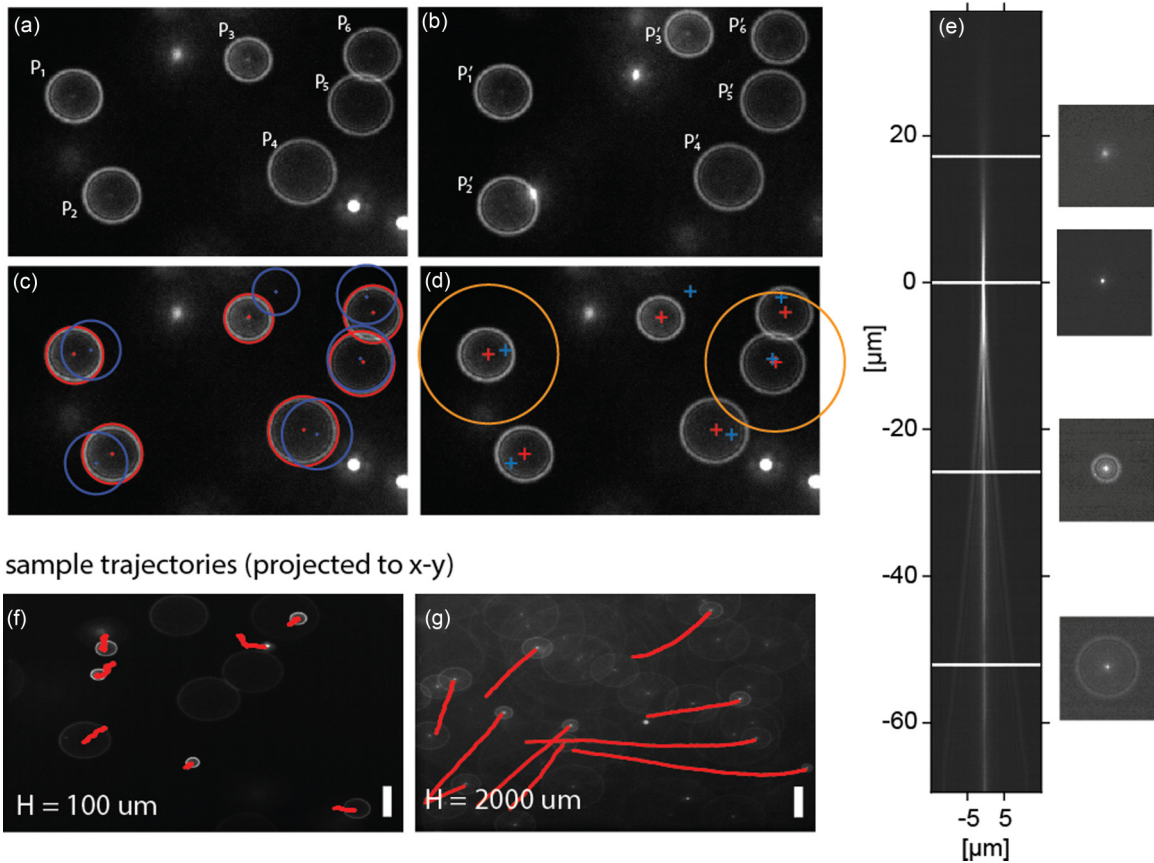
FIG. 1. Example of particle tracking in three dimensions. [(a) and (b)] Raw images taken at two successive times illustrating the sparse seeding of tracer particles. Particle positions are indicated by the Airy rings. (c) The center and size of each ring is detected using Sobel edge detection and the Hough circle transform. (d) Particles are tracked according to a nearest-neighbor algorithm. (e) The z location of each particle is localized using the library of ring sizes vs. distance from the focal plane obtained from a calibration. [(f) and (g)] Two samples of particle tracks, taken from a shallow and a deep test geometry ($H = 100, 2000$ μm) illustrating the qualitative change in particle mobility due to confinement. The scale bar represents 40 μm.

dimensional. In addition, the field of view was enlarged to 700 μm $\times$ 700 μm in the horizontal plane.

Tracer particle trajectories were assembled from a sequence of images using the "nearest-neighbor" method [31] and velocities in all three directions ($u_i = u_x, u_y, u_z$) were calculated using finite differences. Following the turbulence literature [32], velocities were decomposed into mean component and fluctuating component which is a function of experiment time t: $u_i(t) = \bar{u}_i + u'_i(t)$, where $\bar{u}_i$ denotes an average over all particles tracked during a period of constant system activity [$t = 2000$–5600 s, Fig. 3(a)]. The variance of the velocity, $\overline{u'^2_i} \equiv \sigma^2_i = \langle[u_i(t) - \bar{u}_i]^2\rangle$, was computed by averaging over all particles tracked during the same time period.

III. RESULTS AND DISCUSSION

A. Validation of measurement system

To validate the three-dimensional measurement system, we recorded the Brownian motion of fluorescent tracers (1-μm diameter or 2.9-μm diameter) diffusing in deionized (DI) water in three different COC chambers: $H = 4$ mm, $H = 2$ mm,

and $H = 0.1$ mm. The out-of-focus tracers were tracked from frame to frame in three dimensions based on their Airy ring sizes. As expected, the MSD increased linearly with time
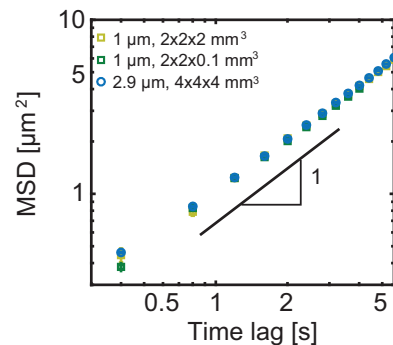

FIG. 2. Normalized mean-square displacements (MSDs) of 1- and 2.9-μm particles diffusing in water and tracked using the Airy-disk three-dimensional tracking technique. The MSDs are normalized by the size of particle (1-μm or 2.9-μm diameter), and the error bars indicate standard errors of the averaging over all tracked particles.
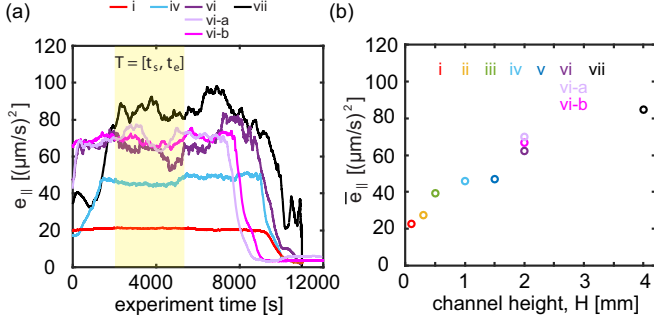
FIG. 3. (a) Lifetime of active systems in varying geometries, indicated by the parallel component of the specific kinetic energy $e_\parallel$. The highlighted area defines a time period, $T = [t_s, t_e]$, over which temporal averaging was calculated. (b) Mean value of parallel component of the specific kinetic energy $\bar{e}_\parallel$. The Roman numerals (i-vii, vi-a, and vi-b) represent different channel geometries (Table I).

(Fig. 2) with normalized slopes of 1.03, 1.00, and 1.07 for diffusion in the 2 mm, 100 μm, and 4 mm test enclosures respectively. The deviation from a slope of one could be due to uncertainty in the tracer particle size or a discrepancy between the fluid temperature in the test chambers and the system temperature sensor, located nearby. The measurements were taken in the midplane of the chamber, at least 50 μm from the nearest solid boundary (in the case of the 100 μm enclosure). For a Newtonian fluid, this is sufficiently far from walls such that there should be no confinement effects [33–35]; as expected, none were observed.

B. Active fluid measurements

To quantify the system dynamics we measured kinetic energy per unit mass, e, as a function of experiment time, t, which was divided into components parallel to ($x - y$: $\parallel$) and perpendicular to (z: $\perp$) the nearest confining boundary. The parallel component $e_\parallel$ is described with velocity component u_x and u_y and the perpendicular component $e_\perp$ with z component of velocity u_z:

$$e(t) = \frac{E(t)}{\frac{1}{2}m} = e_\parallel(t) + e_\perp(t) = \left[u_x^2(t) + u_y^2(t)\right] + u_z^2(t). \quad (1)$$

Since we were not able to measure $e_\perp$ for the largest channel due to the optical limitations, we compare $e_\parallel$ for systems with different levels of confinement [Fig. 3(a)] and observe a consistent behavior: The system evolves quickly to a relatively stable state, remains at that state for approximately 8000–10 000 s, and then decays. Having the same amount of chemical fuel and the same concentration of molecular motors, all the samples exhibited comparable lifetimes independent of confinement size. This suggests that the energy consumption rate per unit mass is independent of the system size.

All quantities reported hereafter are computed during the steady-state period between $t = 2000$–5600 [Fig. 3(a), yellow band]. During this time the average value of the kinetic energy $e_\parallel$ increases linearly with chamber height H, starting at about 20 $(\mu m/s)^2$ and reaching a saturation around 80 $(\mu m/s)^2$ [Fig. 3(b)]. This variation in activity as a function of chamber
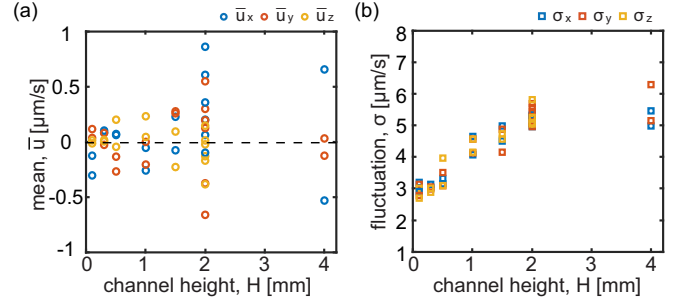

FIG. 4. (a) Mean velocity $\bar{u}_i$ of all tracked particles over the period of $[t_s, t_e]$. Blue: $\bar{u}_x$; red: $\bar{u}_y$; yellow: $\bar{u}_z$. (b) Velocity fluctuation strength σ_i of all tracked particles over the period of $[t_s, t_e]$. Blue: σ_x; red: σ_y; yellow: σ_z. Duplicate symbols represent two repeated tests in identical geometries.

height is evident in the motion of the tracer particles (Figs. 1(f) and 1(g); Supplemental Material videos SV1 and SV2 [30]).

The time-averaged mean velocities in the x, y, and z directions exhibit no long-time sustained large-scale coherent flows [Fig. 4(a)], in contrast to those previously observed in droplets or "race-track" geometries [22,36]. In addition, the individual components of the velocity fluctuations, σ_i ($\sigma_i = \sigma_x, \sigma_y, \sigma_z$) are isotropic [Fig. 4(b)], exhibiting no preferred orientation and no evidence of sustained coherent motion, reinforcing the idea that these fluctuations are generated at the smallest scales and that the filaments are, on average, randomly oriented. This is in contrast to the studies of similar active fluids that were highly confined using an oil surface or a hard wall [13,19] or systems that exhibit local nematic order near walls [22] or systems that are liquid crystals in nematic phase [19,37].

We compute the scaled MSDs of tracers in x-y plane and z axis:

$$\text{MSD}_\parallel = \frac{\langle [x(t + \Delta t) - x(t)]^2 + [y(t + \Delta t) - y(t)]^2 \rangle}{(\sigma_x^2 + \sigma_y^2)\Delta t_o^2},$$

$$(2a)$$

$$\text{MSD}_\perp = \frac{[z(t + \Delta t) - z(t)]^2}{\sigma_z^2 \Delta t_o^2}, \quad (2b)$$

where Δt represents time difference in calculating displacements and Δt_o is 0.1 s relating to image frame rate 10 Hz. The normalization accounts for different levels of activity at each confinement. The mean-square displacement curves exhibit multiple regimes transitioning from subdiffusive or diffusive to superdiffusive (including ballistic) behavior with increasing time lag Δt [Figs. 5(a) and 5(b)]. The dashed lines indicates cross over time lag where the slope of scaled MSD equals 1. In the parallel MSD, subdiffusion is observed only in the most confined system, transitioning to a diffusive behavior at $\Delta t \sim 0.6$ s. In contrast, the wall-normal MSD, transitions from subdiffusive to diffusive are observed for wider range of confinements, with the subdiffusive regime present in all systems with $H \leqslant 1$ mm, and with the crossover time increasing as the confinement increases. This subdiffusive MSD may be associated with the frustration of particle motion at the smallest scales by the microtubule network, which becomes increasingly compressed in the wall-normal direction by the
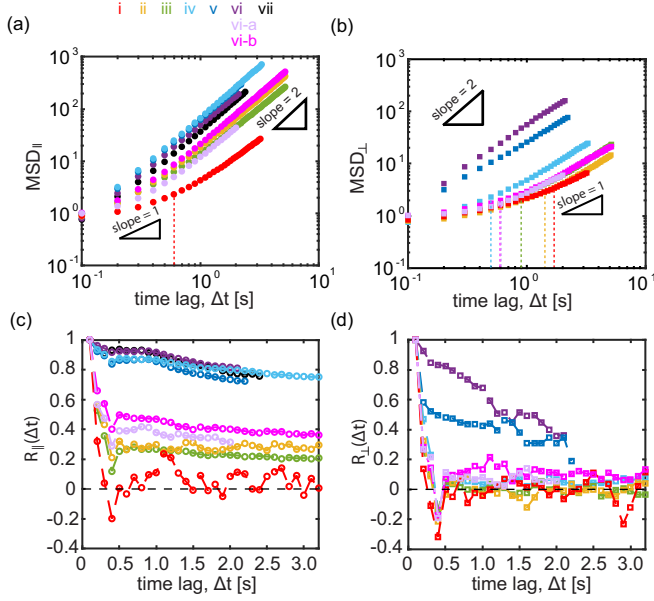
FIG. 5. [(a) and (b)] Scaled mean-square displacements of tracers in the x-y plane (MSD$_\parallel$) and in the z direction (MSD$_\perp$) in different geometries. Two repeated experiments from the same geometry are averaged together. Dashed lines indicate the crossover time as slope equals 1. [(c) and (d)] Velocity-velocity temporal correlation in x-y plane and in z direction from different geometries. The Roman numerals (i-vii, vi-a, and vi-b) represent different channel geometries (Table I).

confining boundaries. However, this remains to be explored further.

Velocity-velocity correlations, defined parallel and perpendicular to the confining walls were also calculated:

$$R_\parallel(\Delta t) = \frac{\langle \mathbf{u}_\parallel(t) \cdot \mathbf{u}_\parallel(t + \Delta t)\rangle}{\langle \mathbf{u}_\parallel(t) \cdot \mathbf{u}_\parallel(t + \Delta t_o)\rangle}, \tag{3a}$$

$$R_\perp(\Delta t) = \frac{\langle \mathbf{u}_\perp(t) \cdot \mathbf{u}_\perp(t + \Delta t)\rangle}{\langle \mathbf{u}_\perp(t) \cdot \mathbf{u}_\perp(t + \Delta t_o)\rangle}. \tag{3b}$$

Here $\mathbf{u}_\parallel(t) = (u_x(t), u_y(t), 0)$ is the horizontal velocity vector and $\mathbf{u}_\perp(t) = (0, 0, u_z(t))$ is the vertical velocity component. We choose not to normalize by the zero-time separation because in a purely thermal motion, where there is no temporal correlation, this leads to a very large discrepancy between the correlation at $\Delta t = 0$ and all other times, $\Delta t \neq 0$. The trends that were observed in the MSDs are also observed in the velocity-velocity (Lagrangian) self-correlations of flow tracers [Figs. 5(c) and 5(d)]. In strong confinement, the temporal correlations drop almost immediately to zero, indicating diffusive behavior in which flow tracers quickly lose any memory of their motion, in agreement with the behavior observed in the diffusion-dominated MSDs and suggests a lack of any large-scale advective structures in strong confinement. The differences between the perpendicular and parallel correlations $R_\perp$, $R_\parallel$, echo the above observation that superdiffusion is suppressed in the direction normal to the confining walls. For taller test chambers ($H \geqslant 1$ mm), $R_\parallel$ exhibits a long-lasting positive correlation while $R_\perp$ changes gradually from a flow with a strong long-time coherence to one with almost no

correlation [Figs. 5(c) and 5(d)]. Both of these trends agree with the observed ballistic motion and superdiffusion in the scaled MSDs. The long-lasting temporal correlations suggest the presence of coherent eddies in the system that continue with a primary direction and magnitude for multiple seconds and which dominate over the random small-scale uncorrelated motion associated with individual filament motion that characterizes the flow under strong confinement. The absence of average velocities or long-time advective transport implies that in these geometries, unlike the cylindrical or "race-track" geometries [22], any coherent eddies or "rivers" are not sustained for a long time, or if they are, then they reorient frequently so that the correlation eventually decays. However, the finite field of view of the measurement does not allow for long-enough tracking of a tracer that is required to capture this reorientation and/or eddy breakup.

The coherent structure of the flow can be assessed using the spatial, particle-particle, correlation in the horizontal plane:

$$C_\parallel(\Delta r) = \frac{\langle \mathbf{u}_\parallel(\mathbf{r}, t) \cdot \mathbf{u}_\parallel(\mathbf{r} + \Delta r, t)\rangle}{\langle \mathbf{u}_\parallel(\mathbf{r}, t) \cdot \mathbf{u}_\parallel(\mathbf{r} + \Delta r_o, t)\rangle}, \tag{4}$$

where $\mathbf{u}_\parallel(\mathbf{r}, t) = (u_x(\mathbf{r}, t), u_y(\mathbf{r}, t), 0)$ is the parallel velocity director, Δr is the horizontal separation $\Delta r = \sqrt{\Delta x^2 + \Delta y^2}$ and the averaging is performed over all equal-time particle pairs in the time window $[t_s, t_e]$. As with the temporal correlations, the spatial correlation is normalized by the value of $C_\parallel$ at a fixed separation Δr_o (~ 30 μm). Since particle tracking is limited to a ~ 40 μm slab in the z direction, neither a meaningful perpendicular component of the spatial correlation $C_\perp$ nor a fully three-dimensional spatial correlation can be calculated. The number of particle pairs used to compute the spatial correlation ranged from $\sim 1.4 \times 10^6$ (case vii, $\Delta r = 30$ μm) to $\sim 6.5 \times 10^4$ (case ii, $\Delta r = 380$ μm) but in all cases was sufficient to ensure a statistically meaningful value of $C_\parallel(\Delta r)$.

The correlation function of an ATP-depleted ("dead") system in an $H = 2$ mm cube drops immediately in a passive system [Fig. 6(a), brown circles]. In comparison, active systems exhibit an extended correlation that decays to zero, but whose characteristic length scale depends on the system size [Fig. 6(a)]. To quantify this, we fit an exponential function to the data:

$$C_\parallel(\Delta r) \approx A e^{b\Delta r}, \tag{5}$$

and extrapolate the fitted function from Δr_o to $+\infty$. Integrating the curve yields a correlation length, $l_c = -A/b e^{b\Delta r_o}$. As the channel height increases [cases (i)–(vii)], the correlation length l_c initially grows rapidly, appearing to asymptote to ~ 400 μm for largest confinements considered. The measured correlation lengths were close to half of the confinement scale for smallest geometries, H, while for the largest confinements they were less than one tenth of the system size. For the $H = 2$ mm cubic confinement, these dynamics were measured at three different distances, Δz, from the wall (cases vi-a, vi-b, and vi). The correlation length l_c increased as the observation location moved away from the wall and toward the geometric center of the test chamber. Cases vi-a and i were observed at the same distance, Δz, from the boundary/boundaries; however, case vi-a was confined by one wall (single-wall) while case i by two walls (double wall).
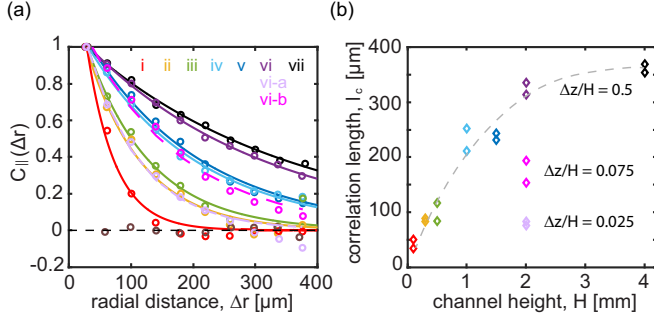
FIG. 6. (a) Normalized equal-time spatial velocity-velocity correlation as a function of separation distance for varying confinements. Circles denote average spatial correlation function measured from two duplicate experiments in each geometry and solid lines present exponential fitting. Brown circles specify the correlation in an ATP-depleted ("dead") system measured in a 2-mm cubic channel. Solid lines indicate exponential fit to the data. (b) Estimated correlation length as a function of channel height computed from the exponential fits. Duplicate symbols represent two repeated tests in identical geometries. The gray dotted line is solely to guide the eye for the measurements made at the center plane of the channel, $\Delta z / H \sim 0.5$. The Roman numerals (i–vii, vi-a, and vi-b) represent different channel geometries (Table I).

A similar comparison exists between cases vi-b and ii. Comparing the single-wall and double-wall confinement with the same Δz (cases vi-a and i and cases vi-b and ii) reveals that the two-wall confinements exhibited even smaller correlation lengths.

Long-ranged correlation lengths demonstrate the existence of confinement-size-dependent characteristic eddies in the active flow that are both much larger than the $\sim$1-μm constituent microtubule filament length and considerably smaller than the shortest distance to a confining surface. Comparing with other systems using kinesin motors confined to $\sim$50–100 μm height geometries, similar correlation functions were observed [20,21,38]. For the largest sized chambers, the correlation length, l_c saturates at $\sim$400 μm suggesting the existence of an maximum intrinsic length scale for this active system. Although the correlation length is consistent with the existence of the "vortexlike" flow structures that were described by Sanchez *et al.* [19] and Henkin *et al.* [20], the shape of the spatial correlation [Fig. 6(a)] seems to be at odds with this view, as a vortex structure should also result in a negative correlation at some distance, reflecting the return flow of the coherent structure. A possible explanation for this is that the structures we see here are randomly oriented 3D vortices and the correlation, $C_\parallel$, averages over all possible horizontal projections, thus the anticorrelated flow is washed out and not visible in the statistics. In the largely unconfined systems, these vortical structures are long-lived until they dissipate and reform (or simply rotate) with a different orientation. Thus we observe highly correlated temporal correlations [Figs. 5(c) and 5(d)], superdiffusive and ballistic scaled MSDs [Figs. 5(a) and 5(b)], high-level specific kinetic energy [Fig. 3(a)], and stronger activity fluctuations [Figs. 4(b)]. Conversely, in the highly confined geometries, the large vortical structures cannot sustain themselves and are

replaced by smaller, randomly oriented, flow structures with short correlation lengths [Fig. 6(b)] and short lifetimes. In this limit we observe a fast decay in the spatial correlation [Fig. 6(a)], a rapid drop in the temporal correlation [Figs. 5(c) and 5(d)], subdiffusive and diffusive scaled MSDs for short time lags [Figs. 5(a) and 5(b)], lower specific kinetic energy [Fig. 3(a)], and weaker activity fluctuation [Fig. 3(b)].

IV. CONCLUSIONS

Vortexlike structures have been observed in numerous confined active systems, including cytoskeletal networks, living cells, and bacterial suspensions [7,10,39–42]. In the kinesin-microtubule system these long-ranged vortex structures have been observed in highly confined systems [19]. Here we extend those observations, observing that the correlation scale increases as the wall effects recede. Although there is the strong suggestion of a saturation in the correlation length [Fig. 6(b)], this is in contrast to recent theories and experiments that suggest the boundaries influence the system at every length scale [43]. Although we see evidence of saturation at our largest system scale ($H = 4$ mm), it is natural to ask if this trend will hold up as the confinement level decreases even more, as well as in geometries in which the aspect ratio between the confined and unconfined axes is consistently maintained at a high value. Unfortunately, these experiments were not available to us due to limitations in the availability of the precious kinesin-microtubule materials, although we expect that more experiments in even larger geometries as well as additional computations will be able to resolve this issue.

The results also raise other questions that remain to be addressed with further experiments. The present analysis is based on the initial 3600 s of the system's activity—around one third of the total system lifetime (more recent kinesin-microtubule systems have demonstrated lifetimes in excess of 70 000 s [21]). A natural question is whether the active fluid has reached a steady state. For instance, if the confinement geometry, or the constituents of the active fluid are changed, then is it possible for stable coherent flows (similarly to Ref. [22]) to emerge, perhaps through some kind of instability [43]. These questions can be addressed in the future by extending the analysis to cover longer times, as well as observing the structure of the microtubule motion simultaneously with the passive tracer transport.

A second critical unknown is how the surface boundary condition might influence the observed results. Different chemical treatments of the surface affect microtubule adhesion, orientation, order, and motion and will likely affect the system lifetime, as well as the velocity patterns and correlations in the interior, especially in the highly confined geometries. This, too, must be addressed in follow-up experiments by careful control and variation in the surface chemistry. Numerical simulations (e.g. Ref. [23]) will also be of great value in answering these questions. Last, these results are specific to the kinesis-microtubule active system, and the applicability to other active systems, for example, those driven by bacterial suspensions [41,42], remains to be explored.

APPENDIX A: MATERIAL PREPARATION DETAILS

Raw tubulin is purified from bovine brains through two cycles of polymerization-depolymerization in high-salt 1 M 1,4-piperazinediethanesulphonic (PIPES) buffer at pH 6.8 and stored at $-80\,^{\circ}$C [44]. Before fluorescent labeling or mixing with molecular motors, raw tubulin is recycled for a third time polymerization-depolymerization and flash-frozen by liquid nitrogen at a high concentration (usually larger than 20 mg/ml and 44.9 mg/ml in this case) using thin-walled tubes. For fluorescent microscopy, a portion of recycled tubulin at high concentration is labeled with Alexa Fluor 568 (Thermal Fisher Scientific, A20003) by a succinimidyl ester linker. Spectrum absorbance indicated that 34% of tubulin monomers are labeled. To prepare microtubule for the active fluids mixture, recycled tubulins (not fluorescent) are copolymerized with Alexa 568 labeled tubulins at $37\,^{\circ}$C for 30 min to produce microtubules with 3% label percentage. For encouragement of polymerization, 600 μM GMPCPP (guanosine-5'-[(α, β)-methyleno]triphosphate; Jena Biosciences, NU-4056) and 1 mM dithiothreital (DTT) and M2B buffer is added to target polymerization concentration at 8 mg/ml. The polymerization concentration can affect polymerization speed and final length of microtubule filaments. The resulting length has an average value of ~ 1 μm [19,22]. Microtubules are stored in small aliquots of 10 μl at $-80\,^{\circ}$C.

We use K401 derived from *Drosophila melanogaster* kinesin, which consists of 401 amino acids of the N-terminal motor domain with a biotin tag [45]. The biotin tag helps to assemble kinesin motors to multimotor clusters using streptavidin tetramers (Invitrogen, S-888). Linking kinesins into motor clusters permits binding among multiple microtubule filaments and introduces interfilament sliding. The mixing ratio of kinesin motors (1.5 μM) and streptavidin (1.8 μM) is 1 : 1.2 in M2B buffer (M2B: 80 mM PIPES, 1 mM EGTA, 2 mM MgCl$_2$, pH 6.8); 120 μM DTT is added before 30 min incubation at $4\,^{\circ}$C. After preparation, the kinesin-straptavidin mixture is stored in aliquots at $-80\,^{\circ}$C.

Microtubules and motor clusters are prepared separately and combined with other mixtures in a high-salt buffer (M2B + 3.9 mM MgCl$_2$). We add an ATP regeneration system, as the most important energy supply for motor clusters, using 26 mM phosphoenolpyruvate (PEP) and 2.8% (v/v) stock pyruvate kinase (PK)/lactic dehydrogenase enzymes (Sigma, P0294). Motor clusters hydrolyze ATP to ADP while stepping on microtubule filaments. PK consumes PEP and converts ADP back to ATP; therefore, the ATP concentration in the active systems remain stable until PEP and ATP are depleted. To reduce photobleaching effect, we minimize the oxygen exposure of fluorescent samples by adding 2 mM trolox (Sigma, 238813) and antioxidants, including 0.22 mg/ml glucose oxidase (Sigma, G2133), 0.038 mg/ml catalase (Sigma, C40), and 3.3 mg/ml glucose. We add 5.5 mM DTT to stabilize proteins, 2% (w/w) Pluronic F127 to force microtubule filaments into bundles and $\sim 0.001\%$ (v/v) fluorescent particles to probe the active systems. The final concentration of microtubules is 1.3 mg/ml, kinesin is 1.5 μM, and ATP is 1.4 mM.

APPENDIX B: MICROCHANNEL CHANNEL SURFACE PREPARATION

To ensure a consistent surface, a standard procedure was followed:

(1) Immerse and sonicate silicon channels for 5 min in boiled 1% (v/v) Hellmanex in DI water.

(2) Rinse sonicated devices thoroughly in DI water and then soak them in ethanol for 10 minutes.

(3) Rinse devices thoroughly in DI water and soak them in 1 M KOH solution for 10 minutes.

(4) Prepare silane solution: 100 ml ethanol, 1 ml acetic acid, and 0.5 ml trimethoxysilyol-propyl methacrylate [H$_2$C $=$ C(CH$_3$)CO$_2$(CH$_2$)3Si(OCH$_3$)$_3$].

(5) Rinse devices thoroughly in DI water and immerse them in silane solution for 10 to 20 min.

(6) Prepare acrylamide solution. We used 20% acrylamide solution and dilute it to 2% with DI water. Then place 2% acrylamide solution in vacuum chamber to degas for 10 minutes.

(7) Take devices out from silane solution, rinse them with DI water, and blow dry them with compressed nitrogen (or compressed air).

(8) Polymerize acrylamide. Take acrylamide solution out from the vacuum chamber. Mix 100 ml 2% acrylamide solution with 70 mg ammonium persulfate (APS) and 35 μl tetramethylethylenediamine (TEMED). Note: Let the APS dissolve first while stirring and then add TEMED. Volume and mass can be linearly increased if larger volume of polyacrylamide solution in need.

(9) Within 20 s after adding TEMED, immerse dry devices into polymerized acrylamide solution. Coating should be ready in ~ 3 h.

[1] R. D. Vale, T. S. Reese, and M. P. Sheetz, Cell **42**, 39 (1985).

[2] J. Gelles, B. J. Schnapp, and M. P. Sheetz, Nature **331**, 450 (1988).

[3] J. Howard, A. Hudspeth, and R. Vale, Nature **342**, 154 (1989).

[4] R. Urrutia, M. A. McNiven, J. P. Albanesi, D. B. Murphy, and B. Kachar, Proc. Natl. Acad. Sci. USA **88**, 6701 (1991).

[5] A. J. Hunt, F. Gittes, and J. Howard, Biophys. J. **67**, 766 (1994).

[6] M. J. Schnitzer and S. M. Block, Nature **388**, 386 (1997).

[7] F. Ndlec, T. Surrey, A. C. Maggs, and S. Leibler, Nature **389**, 305 (1997).

[8] M. Pinot, F. Chesnel, J. Kubiak, I. Arnal, F. Nedelec, and Z. Gueroui, Curr. Biol. **19**, 954 (2009).

[9] V. Schaller, C. Weber, C. Semmrich, E. Frey, and A. R. Bausch, Nature **467**, 73 (2010).

[10] Y. Sumino, K. H. Nagai, Y. Shitaka, D. Tanaka, K. Yoshikawa, H. Chaté, and K. Oiwa, Nature **483**, 448 (2012).

[11] Y. H. Tee, T. Shemesh, V. Thiagarajan, R. F. Hariadi, K. L. Anderson, C. Page, N. Volkmann, D. Hanein, S. Sivaramakrishnan, M. M. Kozlov *et al.*, Nat. Cell Biol. **17**, 445 (2015).

[12] M. Miyazaki, M. Chiba, H. Eguchi, T. Ohki, and S. Ishiwata, Nat. Cell Biol. **17**, 480 (2015).

[13] A. Opathalage, M. M. Norton, M. P. Juniper, B. Langeslay, S. A. Aghvami, S. Fraden, and Z. Dogic, Proc. Natl. Acad. Sci. USA **116**, 4788 (2019).

[14] K. E. Sawin, K. LeGuellec, M. Philippe, and T. J. Mitchison, Nature **359**, 540 (1992).

[15] T. Wittmann, A. Hyman, and A. Desai, Nat. Cell Biol. **3**, E28 (2001).

[16] W. E. Theurkauf, Science **265**, 2093 (1994).

[17] H. Ueda, E. Yokota, N. Kutsuna, T. Shimada, K. Tamura, T. Shimmen, S. Hasezawa, V. V. Dolja, and I. Hara-Nishimura, Proc. Natl. Acad. Sci. USA **107**, 6894 (2010).

[18] J. Brugués and D. Needleman, Proc. Natl. Acad. Sci. USA **111**, 18496 (2014).

[19] T. Sanchez, D. T. Chen, S. J. DeCamp, M. Heymann, and Z. Dogic, Nature **491**, 431 (2012).

[20] G. Henkin, S. J. DeCamp, D. T. Chen, T. Sanchez, and Z. Dogic, Philos. Trans. R. Soc., A **372**, 20140142 (2014).

[21] P. Chandrakar, J. Berezney, B. Lemma, B. Hishamunda, A. Berry, K.-T. Wu, R. Subramanian, J. Chung, D. Needleman, J. Gelles *et al.*, arXiv:1811.05026.

[22] K.-T. Wu, J. B. Hishamunda, D. T. Chen, S. J. DeCamp, Y.-W. Chang, A. Fernández-Nieves, S. Fraden, and Z. Dogic, Science **355**, eaal1979 (2017).

[23] M. Varghese, A. Baskaran, M. F. Hagan, and A. Baskaran, Phys. Rev. Lett. **125**, 268003 (2020).

[24] F. Hilitski, A. R. Ward, L. Cajamarca, M. F. Hagan, G. M. Grason, and Z. Dogic, Phys. Rev. Lett. **114**, 138102 (2015).

[25] M. Born and E. Wolf, *Principles of Optics: Electromagnetic Theory of Propagation Interference and Diffraction of Light*, 6th ed. (Pergamon Press, London, 1980).

[26] E. Afik, Sci. Rep. **5**, 13584 (2015).

[27] K. Taute, S. Gude, S. Tans, and T. Shimizu, Nat. Commun. **6**, 8776 (2015).

[28] N. Kanopoulos, N. Vasanthavada, and R. L. Baker, IEEE J. Solid-State Circuits **23**, 358 (1988).

[29] D. H. Ballard, Pattern Recognit. **13**, 111 (1981).

[30] See Supplemental Material at http://link.aps.org/supplemental/10.1103/PhysRevE.104.034601 for videos of tracer particles moving in active fluids.

[31] R. J. Adrian and J. Westerweel, *Particle Image Velocimetry*, 30 (Cambridge University Press, Cambridge, UK, 2011).

[32] H. Tennekes and J. L. Lumley, *A First Course in Turbulence* (MIT Press, Cambridge, MA, 1972).

[33] J. Happel and H. Brenner, *Low Reynolds Number Hydrodynamics: With Special Applications to Particulate Media*, Vol. 1 (Springer Science & Business Media, New York, 2012).

[34] B. Lin, J. Yu, and S. A. Rice, Phys. Rev. E **62**, 3909 (2000).

[35] P. Huang and K. S. Breuer, Phys. Rev. E **76**, 046307 (2007).

[36] K. Suzuki, M. Miyazaki, J. Takagi, T. Itabashi, and S. I. Ishiwata, Proc. Natl. Acad. Sci. USA **114**, 2922 (2017).

[37] A. Hitt, A. Cross, and R. Williams, J. Biol. Chem. **265**, 1639 (1990).

[38] L. M. Lemma, S. J. DeCamp, Z. You, L. Giomi, and Z. Dogic, Soft Matter **15**, 3264 (2019).

[39] I. H. Riedel, K. Kruse, and J. Howard, Science **309**, 300 (2005).

[40] C. Dombrowski, L. Cisneros, S. Chatkaew, R. E. Goldstein, and J. O. Kessler, Phys. Rev. Lett. **93**, 098103 (2004).

[41] J. Dunkel, S. Heidenreich, K. Drescher, H. H. Wensink, M. Bär, and R. E. Goldstein, Phys. Rev. Lett. **110**, 228102 (2013).

[42] V. A. Martinez, E. Clément, J. Arlt, C. Douarche, A. Dawson, J. Schwarz-Linek, A. K. Creppy, V. Škultéty, A. N. Morozov, H. Auradou, and W. C. K. Poon, Proc. Natl. Acad. Sci. USA **117**, 2326 (2020).

[43] P. Chandrakar, M. Varghese, S. A. Aghvami, A. Baskaran, Z. Dogic, and G. Duclos, Phys. Rev. Lett. **125**, 257801 (2020).

[44] M. Castoldi and A. V. Popov, Protein Expression Purif. **32**, 83 (2003).

[45] T.-G. Huang and D. D. Hackney, J. Biol. Chem. **269**, 16493 (1994).